Global empirical model for mapping zenith wet delays onto precipitable water

Yi Bin Yao, Bao Zhang, Shun Qiang Yue, Chao Qian Xu & Wen Fei Peng

Journal of Geodesy
Continuation of Bulletin Géodésique and manuscripta geodaetica

ISSN 0949-7714
Volume 87
Number 5

J Geod (2013) 87:439-448
DOI 10.1007/s00190-013-0617-4

Springer

Your article is protected by copyright and all rights are held exclusively by Springer-Verlag Berlin Heidelberg. This e-offprint is for personal use only and shall not be self-archived in electronic repositories. If you wish to self-archive your article, please use the accepted manuscript version for posting on your own website. You may further deposit the accepted manuscript version in any repository, provided it is only made publicly available 12 months after official publication or later and provided acknowledgement is given to the original source of publication and a link is inserted to the published article on Springer's website. The link must be accompanied by the following text: "The final publication is available at link.springer.com".

Author's personal copy

J Geod (2013) 87:439–448
DOI 10.1007/s00190-013-0617-4

ORIGINAL ARTICLE

Global empirical model for mapping zenith wet delays onto precipitable water

Yi Bin Yao · Bao Zhang · Shun Qiang Yue · Chao Qian Xu · Wen Fei Peng

Received: 26 June 2012 / Accepted: 29 January 2013 / Published online: 20 February 2013
© Springer-Verlag Berlin Heidelberg 2013

Abstract We can map zenith wet delays onto precipitable water with a conversion factor, but in order to calculate the exact conversion factor, we must precisely calculate its key variable T_m. Yao et al. (J Geod 86:1125–1135, 2012. doi:10.1007/s00190-012-0568-1) established the first generation of global T_m model (GTm-I) with ground-based radiosonde data, but due to the lack of radiosonde data at sea, the model appears to be abnormal in some areas. Given that sea surface temperature varies less than that on land, and the GPT model and the Bevis T_m–T_s relationship are accurate enough to describe the surface temperature and T_m, this paper capitalizes on the GPT model and the Bevis T_m–T_s relationship to provide simulated T_m at sea, as a compensation for the lack of data. Combined with the T_m from radiosonde data, we recalculated the GTm model coefficients. The results show that this method not only improves the accuracy of the GTm model significantly at sea but also improves that on land, making the GTm model more stable and practically applicable.

Electronic supplementary material The online version of this article (doi:10.1007/s00190-013-0617-4) contains supplementary material, which is available to authorized users.

Y. B. Yao (✉) · B. Zhang · S. Q. Yue · C. Q. Xu · W. F. Peng
School of Geodesy and Geomatics, Wuhan University, Wuhan 430079, China
e-mail: ybyao@whu.edu.cn

B. Zhang
e-mail: whusggzb@gmail.com

S. Q. Yue
e-mail: shqyue@whu.edu.cn

C. Q. Xu
e-mail: cqxu@whu.edu.cn

W. F. Peng
e-mail: sggwfpeng@126.com

Keywords GPS meteorology · Zenith wet delay · Precipitable water

List of abbreviations

COSMIC	Constellation Observation System of Meteorology, Ionosphere, and Climate
GPS	Global Positioning System
GPT	Global Pressure and Temperature
GTm	Global T_m model
GNSS	Global Navigation Satellite System
ECMWF	European Centre for Medium-Range Weather Forecasts
IGRA	Integrated Global Radiosonde Archive
MAE	Mean Absolute Error
PWV	Precipitable Water Vapor
RMS	Root Mean Square
ZWD	Zenith Wet Delay

1 Introduction

As an important component of the Earth's atmosphere, water vapor is mainly distributed at the bottom of the troposphere, constituting approximately 99 % of water vapor total content. Although little water vapor exists in the atmosphere, it is one of the most active and variable parts among the atmospheric components and one of the most difficult meteorological parameters to characterize (Rocken et al. 1993). Water vapor plays a key role in a range of spatial and temporal scales of atmospheric processes and its distribution is directly related to the distribution of clouds and precipitation. Meanwhile, water vapor is the most abundant and important

Author's personal copy

greenhouse gas in the Earth's atmosphere. A good understanding of the distribution of water vapor in the atmosphere will be of great assistance in weather forecasting and climate prediction.

Traditional water vapor measurement methods include radiosonde, water vapor radiometer, satellite remote sensing, etc. But due to heavy workload, high equipment costs, or low spatial and temporal resolution, these methods gradually become unable to meet the increasing demands of meteorological development. Using Global Positioning System (GPS) to detect water vapor has become an interesting area of research.

Precipitable water vapor (PWV) has been highlighted in GPS meteorological calculation. By means of specific methods we can estimate zenith wet delays (ZWD) based on GPS observation data, and the relationship between ZWD and PWV can be expressed as (Bevis et al. 1992):

$$\mathrm{PWV} = \Pi \cdot \mathrm{ZWD} \tag{1}$$

where $\prod$ is a water vapor conversion factor. It can be expressed as:

$$\Pi = \frac{10^6}{\rho_w R_v \left[(k_3/T_m) + k_2'\right]} \tag{2}$$

where ρ_w is the density of water, R_v is the specific gas constant for water vapor, k_2', k_3 are the atmospheric refractivity constants (Davis et al. 1985; Bevis et al. 1994), T_m is the key variable to calculate the conversion factor Π.

T_m is an important parameter in ground-based GPS meteorology, which is usually expressed as a linear function of surface temperature T_s. Various scientists have made many achievements in exploring the linear relationship between T_m and T_s. Bevis et al. (1992) came up with the equation $T_m = 70.2 + 0.72\ T_s$, which is suitable for use at mid-latitudes, based on analysis of 8,718 radiosonde profiles. Since not all GPS stations possess the ability to measure the surface temperature, application of the formula has been limited. Based on the analysis of 23 years of radiosonde data from 53 stations, Ross and Rosenfeld (1997) noted that the T_m–T_s relationship changes with station locations and seasons. Generally, the correlation between T_m and T_s weakens in the equatorial region, and becomes weaker in summer than in winter. Gu et al. (2005) did some research on the T_m variations and regional T_m calculation. Li et al. (2006) verified the applicability of Bevis T_m–T_s relationship in Chengdu areas. Mao (2006) systematically studied the method of using GPS to detect water vapor. Ding (2009) introduced the fundamental of the GPS meteorology and related calculation methods in detail. Many Chinese scientists, such as Li et al. (1999), Liu et al. (2000), Gu (2004), Wang et al. (2007) and Lv et al. (2008), have also established regionally applicable linear models. Considering seasonal variations, Yao et al. (2012) established the globally applicable GTm-I model independent of surface temperature, using radiosonde data of 135 stations in 2005–2009. As the radiosonde stations are all located on land or on a few small islands, there are not enough radiosonde data in the oceanic areas involved in the GTm-I modeling even though EUMETNET, a group of 29 European National Meteorological Services, launches twice daily radiosondes from ships. As a result, when calculating T_m at sea, especially in the eastern Pacific, the accuracy is not guaranteed. To address this problem, the GPT model and the Bevis T_m–T_s relationship were employed in this paper to provide T_m at sea as a compensation for data unavailability. The GTm model coefficients were then recalculated using T_m time series in both oceanic and terrestrial areas.

2 The methods of computing T_m

2.1 Computing T_m from radiosonde and COSMIC data

Radiosonde data include geopotential height H, temperature T and relative humidity (RH) at several specific isobaric surfaces. The relative humidity (RH) can be expressed as:

$$\mathrm{RH} = 100 \cdot \frac{P_v}{P_s} \tag{3}$$

where P_v is the vapor pressure, P_s is the saturation vapor pressure, RH is expressed in percentage. A formula (Yu 2011) for the calculation of saturation vapor pressure is:

$$P_s = 6.105 \cdot \exp\left[25.22 \cdot \frac{T - 273.15}{T} - 5.31 \cdot \ln\frac{T}{273.15}\right] \tag{4}$$

where temperature T and relative humidity RH can be obtained from radiosonde data and vapor pressure P_v can be calculated by Eqs. (3) and (4). T_m can be obtained by using the following discrete integral formula:

$$T_m = \frac{\int \frac{P_v}{T} dz}{\int \frac{P_v}{T^2} dz} = \frac{\sum \frac{P_{vi}}{T_i} \cdot \Delta h_i}{\sum \frac{P_{vi}}{T_i^2} \cdot \Delta h_i} \tag{5}$$

where P_{vi} and T_i are the average vapor pressure and average temperature of the atmosphere at the ith layer respectively and Δh_i is the atmosphere thickness at the ith layer. In the actual data processing, bad radiosonde data of less than 15 layers or observation heights lower than 12 km are excluded to avoid considerable errors. At present, free access to radiosonde data of over 1,000 radiosonde stations for many years is available on the Integrated Global Radiosonde Archive website.

In addition to the radiosonde data, meteorological data provided by COSMIC can also be used to calculate T_m. COSMIC is a project of space science experiments for detecting the atmosphere, customized by the US Department of

Author's personal copy

Defense and Taiwan area at the end of the last century. The COSMIC meteorological data, including temperature, vapor pressure, atmospheric pressure and refractive index at different heights of the atmosphere, can be used to calculate the T_m by Eq. (5). What must be pointed out is that the COSMIC data are not true independent observations. In neutral atmosphere, the atmospheric refractive index is related to temperature, pressure and humidity, and the relationship between them can be expressed as (Kursinski et al. 2002):

$$N = 77.6\frac{P}{T} + 3.73 \times 10^5 \frac{P_w}{T^2} \tag{6}$$

where P is atmospheric pressure(in hpa), T is temperature (in Kelvin), P_w is vapour pressure(in hpa). In dry atmosphere, Eq. (6) can be expressed as:

$$N = 77.6\frac{P}{T} \tag{7}$$

By combining Eq. (7), the ideal gas law and static equilibrium equations, we can get P and T easily. However, when the radio occultation measurements get close to the ground where most of humidity is, it is a particular problem to separate accurate temperature and humidity from a GPS radio occultation profile. For that reason, auxiliary information must be used in the humidity derivation. COSMIC post-processed data, also used in this paper, are the results of using the ECMWF's NWP data to help derive humidity, pressure and vapour pressure from COSMIC observations.

Theoretically, the COSMIC system can provide daily 3,000 profiles of the atmospheric elements worldwide with a relatively high vertical resolution of about 0.5 km and a horizontal resolution of about 300 km. The COSMIC occultations are almost evenly distributed around the world, or more precisely, it is a little denser at mid- and high latitudes than in the equatorial region. However, the small number of satellites in the GNSS and COSMIC systems make the COSMIC's time resolution lower than that of radiosondes. Since the COSMIC radio occultation hardly occurs repeatedly at the same site, it is not easy to get a T_m time series at a certain site over a period of one year to fit T_m's annual average and amplitude. Therefore, the COSMIC profiles are not used in GTm modeling, but in the model's accuracy testing in this paper. In fact, about 473,401 valid COSMIC profiles are involved in the model's accuracy validation.

2.2 Computing T_m according to surface temperature

Bevis et al. (1992) of the University of Hawaii came up with a linear regression formula for use at mid-latitudes based on an analysis of 8,718 radiosonde profiles of 13 sounding stations in the United States:

$$T_m = 70.2 + 0.72T_s \tag{8}$$

The formula is simple and intuitive. Input surface temperature T_s, T_m can be obtained. The model has a root mean square error (RMS) of 4.74 K (Bevis et al. 1992), suitable for most areas of the Northern Hemisphere, and it is also the most widely used model for T_m computation. Since the Bevis T_m–T_s relationship is based on localized radiosonde data, it is still a regional model in essence.

In practical applications, many GPS stations are not equipped with surface temperature measuring equipments, so T_m cannot be calculated based on Eq. (8). Boehm et al. (2007) established the GPT model, which is an empirical model based on 9×9 spherical harmonics, and well solved the problem of deriving surface temperature. If you input a station's three-dimensional coordinates and day of the year, the GPT model can output the pressure and temperature of the station. This indicates that T_m at any point can be simulated with certain accuracy from the combination of the GPT model and the Bevis T_m–T_s relationship.

3 Global T_m model GTm

Yao et al. (2012) thought that T_m is influenced by station's location and time of the year, rather than being in a strict linear relationship with surface temperature T_s. Based on this assumption, they proposed a global T_m model, which can be expressed as:

$$T_m = \alpha_1 + \alpha_2 h + \alpha_3 \cos\left(\frac{\text{doy} - 28}{365.25} 2\pi\right) \tag{9}$$

where α_1 is the annual average of T_m and α_3 is the amplitude. Both are related to locations, while α_2 is T_m lapse rate, h represents height, and doy is the day of the year. From the Eq. (9), we can come to the conclusion that for a specific location, T_m is only related to the day of the year.

If we have a series of T_ms of a specific location on a time scale of more than one year and plug them into Eq. (9), we will obtain simultaneous equations with three unknowns α_1, α_2 and α_3. As these are more than unknowns, we can solve the equations and obtain α_1, α_2 and α_3 by using the least squares method.

We can obtain α_1 and α_3 of different locations by using the method mentioned above, but it is not reasonable to calculate α_1 and α_3 at every point on the earth. So we use spherical harmonics to describe global $\alpha_i (i = 1, 3)$, which are expressed as:

$$\alpha_i = \sum_{n=0}^{9} \sum_{m=0}^{n} P_{nm}(\sin\varphi)(C_{nm}\cos(m\lambda) + S_{nm}\sin(m\lambda)) \tag{10}$$

φ: latitude; λ: longitude; P_{nm}: Legendre functions; C_{nm}, S_{nm}: model coefficients. If $P_{nm}(\sin\varphi) \cdot \cos(m\lambda)$ is replaced by

Author's personal copy

$aP(i)$, $P_{nm}(\sin\varphi)\cdot\sin(m\lambda)$ by $bP(i)$, C_{nm} by atm_mean(i) or atm_amp(i), and S_{nm} by btm_mean(i) or btm_amp(i), Eq. (10) will turn to Eq. (11).

$$\begin{aligned}\alpha_1 &= \sum_{i=1}^{55}[atm\_mean(i)\cdot aP(i) + btm\_mean(i)\cdot bP(i)]\\ \alpha_3 &= \sum_{i=1}^{55}[atm\_amp(i)\cdot aP(i) + btm\_amp(i)\cdot bP(i)]\end{aligned} \tag{11}$$

where atm_mean(i), btm_mean(i), atm_amp(i), btm_amp(i) and $\alpha_2$are the model coefficients, $aP(i), bP(i)$ are the longitude- and latitude-related functions. If we get enough α_1 and α_3 at different points worldwide, we can linearize Eq. (11) and solve for the unknowns atm_mean(i), btm_mean(i), atm_amp(i) and btm_amp(i) in a least squares adjustment, yielding the GTm model.

Considering the uneven distribution of radiosonde stations as well as the fact that some stations do not have sufficient data, 135 stations were finally selected and more than 370,000 radiosonde profiles in 5 years (January 2005–December 2009) from these stations were used to establish the GTm-I model. Taking station locations and seasonal variations into account, the GTm-I model is more rigorous and independent of surface temperature and as accurate as the Bevis T_m–T_s relationship. However, due to the unavailability of sea data in GTm-I modeling, the GTm-I model is inaccurate or even abnormal in some oceanic areas, despite the high accuracy achieved on land. To verify this, we divided the globe evenly into $10^\circ \times 20^\circ$ global grids according to latitude and longitude, and 39 oceanic grids were selected to test the accuracy of the GTm-I model. In these grids, T_m derived from the integration of the COSMIC data was considered as true value, and the mean absolute error (MAE) and RMS of the GTm-I model were calculated. The statistical results are shown in Fig. 1, in which the horizontal axis represents the latitudes of the grids.

Figure 1 shows that selected grids are mainly distributed in oceanic areas in the Southern Hemisphere. And while T_m has a relatively high accuracy in the Northern Hemisphere, it has a low accuracy in the Southern Hemisphere, even becomes abnormal. This could be explained by the fact that the radiosonde stations are mainly distributed in the Northern Hemisphere. The GTm-I model fits well in the Northern Hemisphere but fits poorly in the Southern Hemisphere, indicating that the accuracy and stability of the GTm-I model need to be improved in oceanic areas.

4 Establishing the GTm-II model

Before establishing the GTm-II model, we first assessed the accuracy of the GPT model in calculating temperature, using the $2^\circ \times 2.5^\circ$ temperature data provided daily at 0:00, 6:00, 12:00 and 18:00 UTC in 2010 by ECMWF. We calculated the bias and MAE of the GPT model at every grid point. The mean bias is 1.1 K and the MAE is 3.6 K on a global basis, and it achieves a higher accuracy at mid and low latitudes (N60°–S60°) with a bias of 0.7 K and MAE of 2.7 K.The global distribution of mean error and MAE is shown in Fig. 2.

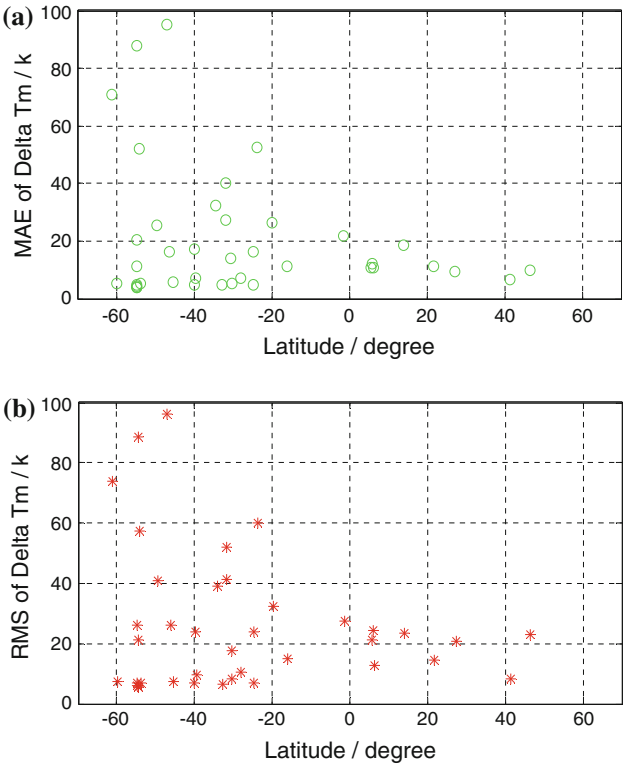

Fig. 1 MAE and RMS of the GTm-I model tested by COSMIC data in some oceanic areas

The statistical data above show that the GPT model has a high accuracy in calculating temperature, especially at mid and low latitudes. Figure 2a and b make it a little more visual that the GPT model agrees well with the ECMWF temperature, especially in the ocean areas.

Considering that surface temperature varies less at sea than on land and the Bevis T_m-T_s relationship is accurate enough to describe the T_m in some areas, we use the GPT model and the Bevis T_m–T_s relationship to simulate T_m as compensation for the absence of data at sea in this paper. First, we divided the globe into $10^\circ \times 20^\circ$ grids evenly. Not counting the 135 radiosonde stations used in the GTm-I modeling, there were 191 grids left without radiosonde data. The 191 stations were mainly distributed in oceanic areas and polar regions, and the center of every grid was considered as a virtual station. The radiosonde stations and virtual stations involved in GTm-II modeling are shown in Fig. 3.

Subsequently, the GPT model was employed to calculate surface temperature T_s of the virtual stations from 2005 to 2009, with a time resolution of 0.5 days. Then, the Bevis

Author's personal copy

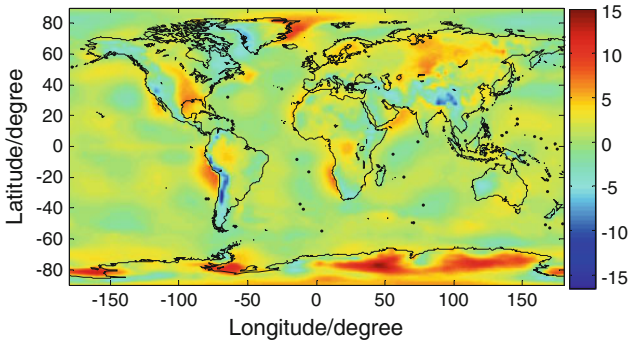

(a) Global distribution of bias

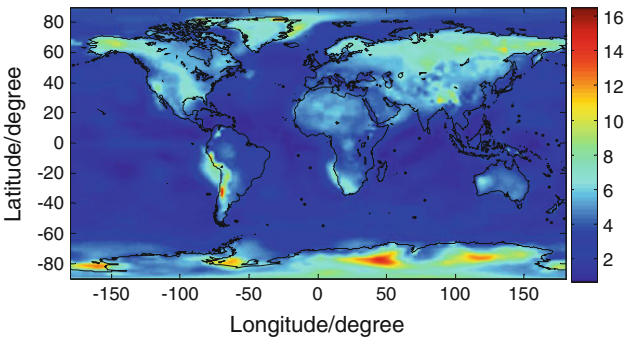

(b) Global distribution of MAE

Fig. 2 The global distribution of bias and MAE of the GPT model compared with ECMWF temperature data

T_m–T_s relationship was adopted to calculate T_m, and approximately 700,000 T_ms of 191 virtual stations were obtained.

Finally, data from the 191 virtual stations and those from the 135 radiosonde stations were combined to recalculate the GTm model coefficients atm_mean(i), btm_mean(i), atm_amp(i), btm_amp(i) and by Eqs. (9) and (11). In this way, the GTm-II model was established. The constant coefficient $\alpha_2 = -0.0060$, and the global distribution of α_1 and α_3 is shown in Fig. 4.

From the comparison of Fig. 4a and c, the deficiencies α_1 of in the GTm-I model are shown to be eliminated in the eastern Pacific and weakened in the Indian Ocean in the GTm-II model. From the comparison of Fig. 4b and d, the deficiencies are shown to have weakened significantly in eastern Pacific and off the east coast of Africa in the GTm-II model. Figure 4a and b shows that the distribution of α_1 and α_3 is smooth, and no abnormalities are observed, indicating that the use of virtual stations in GTm-II modeling effectively suppresses the abnormalities at sea and makes the GTm-II model better conform to the practical case.

5 Validation of GTm-II

In this paper, the accuracy and stability of the models are assessed by MAE and RMS with the following formula:

$$\mathrm{MAE} = \frac{1}{N}\sum_{i=1}^{N}\left(\left|T'_{\mathrm{m}_i} - T_{\mathrm{m}_i}\right|\right) \tag{12}$$

$$\mathrm{RMS} = \sqrt{\frac{1}{N}\sum_{i=1}^{N}\left(\left|\mathrm{T}'_{\mathrm{m}_i} - \mathrm{T}_{\mathrm{m}_i}\right|\right)^2} \tag{13}$$

where T'_{m_i} is the value calculated by the models, T_{m_i} is the true value, and N represents the number of measurements. MAE reflects the mean absolute bias between the calculated values and the true values, and RMS indicates the reliability and stability of the model.

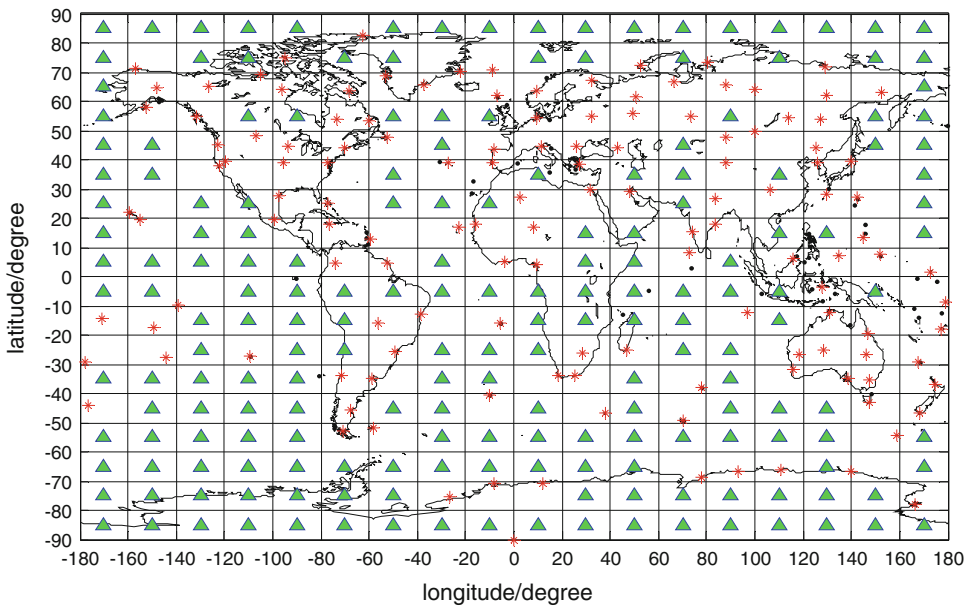

Fig. 3 The distribution of 135 radiosonde stations (*red asterisk*) and 191 virtual stations (*green triangle*) used in GTm-II modeling

Author's personal copy

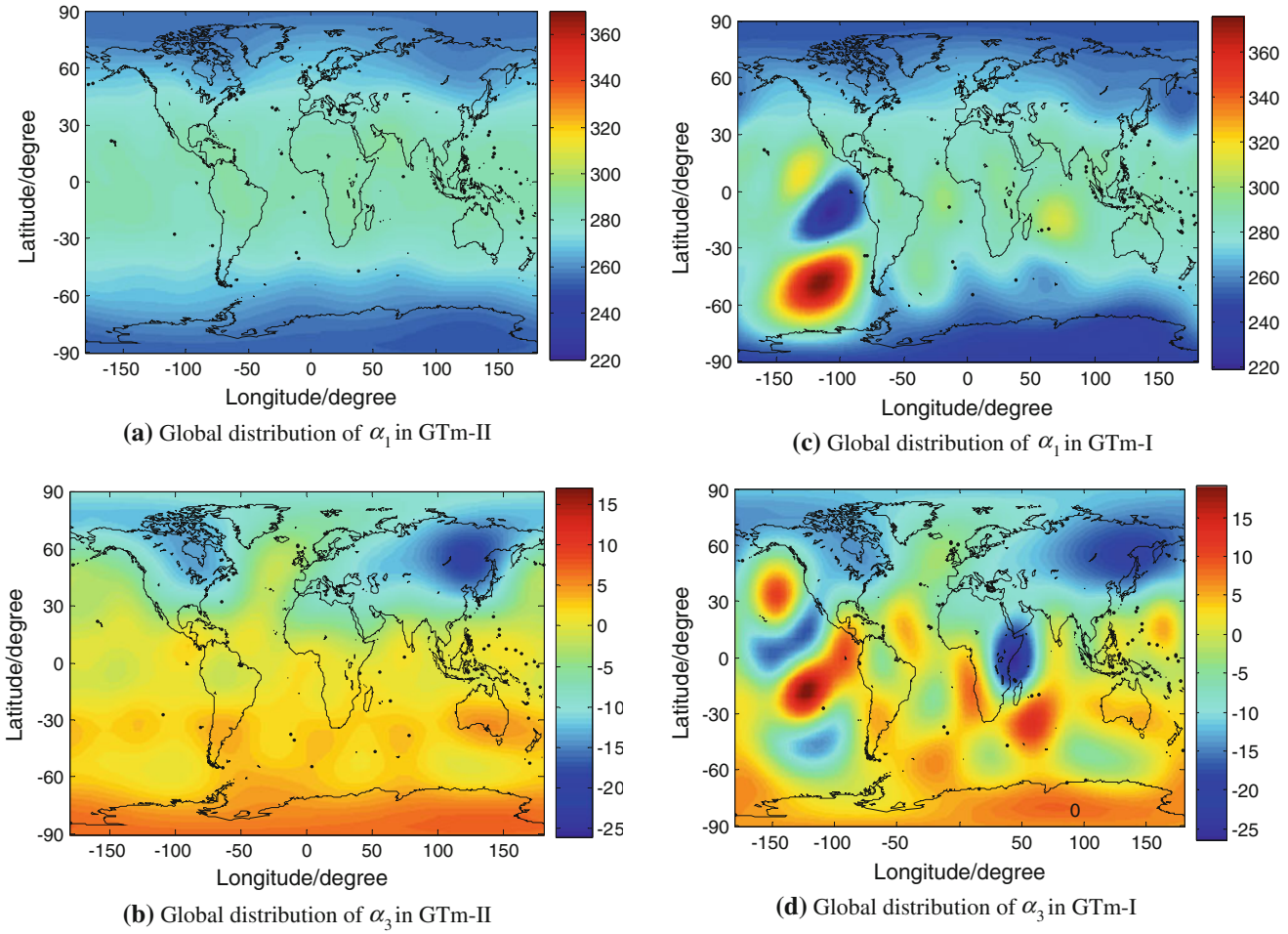

(a) Global distribution of α_1 in GTm-II

(c) Global distribution of α_1 in GTm-I

(b) Global distribution of α_3 in GTm-II

(d) Global distribution of α_3 in GTm-I

Fig. 4 Global distribution of α_1 and α_3 in GTm-I and GTm-II

Due to the unavailability of the true value of T_m, we could only treat the T_m obtained from the integration of the radiosonde data or COSMIC data as the true values.

5.1 Internal accuracy testing

To test the correctness of the GTm-II model, 18 radiosonde stations and 20 virtual stations involved in the modeling were selected. For the radiosonde stations, T_ms from radiosonde data were treated as true values. For the virtual stations, T_ms from the Bevis T_m–T_s relationship (T_s from GPT model) were treated as true values. Then the MAE and RMS of the GTm-II model were calculated. The results are shown in Fig. 5.

Figure 5 shows that the internal accuracy of the GTm-II model is uniform. For the 18 radiosonde stations, MAE $<$ 6 K, RMS $<$ 7 K, and the average RMS is 4.2 K. For the 20 virtual stations, MAE $<$ 3 K, RMS $<$ 3 K. The results show that the MAE and RMS of the GTm-II model are small on land and at sea, indicating that the GTm-II model was well constrained by the radiosonde and virtual observations.

5.2 External accuracy testing

Internal accuracy testing can only prove the rationality and effectiveness of the GTm-II model to some extent. To fully test the reliability and adaptability of the GTm-II model, more stations that were not involved in establishing the model should be used to examine the accuracy of the GTm-II model. Based on Sect. 5.1, 58 radiosonde stations and 39 10° × 20° ocean grids were selected to test the model. T_ms from radiosonde data and COSMIC data were treated as true values, MAE and RMS of the GTm-II model at each radiosonde station or in each ocean grid were calculated.

The statistics of the radiosonde and COSMIC occultation data in 2010 show that each radiosonde station has an average of approximately 500 sounding observations, and each ocean grid has over 2,000 occultation observations. The distribution of the 58 radiosonde stations and 39 ocean grids is shown in Fig. 6. The blue numbers stand for the sequence numbers of the ocean grids, whereas the red "*" represents the radiosonde stations. The test results are shown in Fig. 7.

Author's personal copy

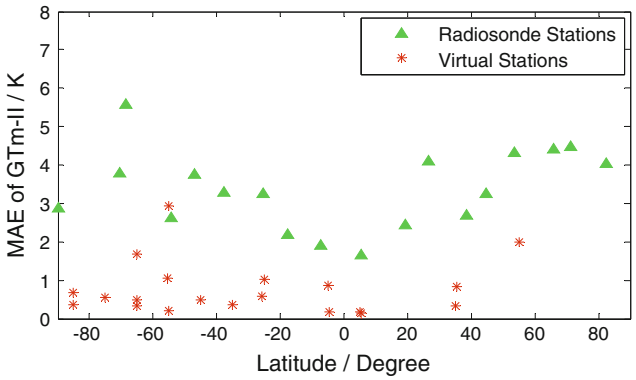

(a) MAE of GTm-II

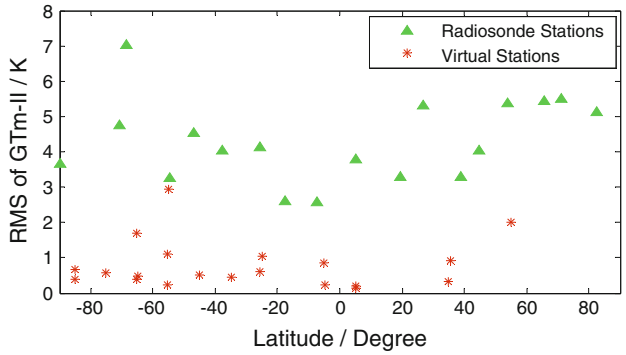

(b) RMS of GTm-II

Fig. 5 Internal accuracy testing results of 18 radiosonde stations and 20 virtual stations involved in G_m-II modeling

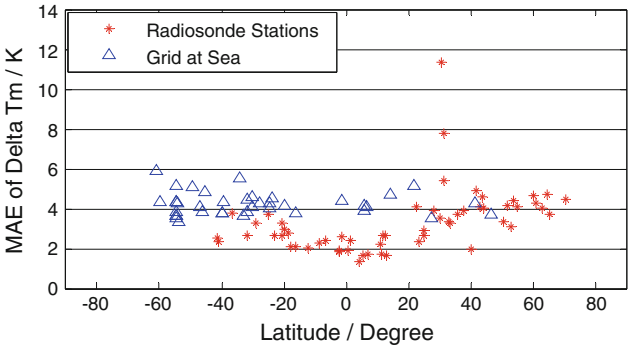

(a) MAE of GTm-II

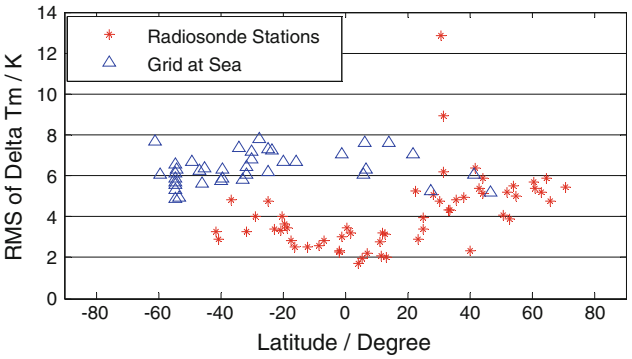

(b) RMS of GTm-II

Fig. 7 External accuracy testing results of 58 radiosonde stations and 39 ocean grids

For ocean grids, the horizontal axis in Fig. 7 represents the latitudes of the center of the grids. Figure 7a shows that most MAEs of the 58 radiosonde stations are less than 4 K, and only 2 stations' MAEs are larger than 6 K. The MAEs of the 39 ocean grids are all less than 6 K. The MAEs in oceanic areas are slightly larger than that on land, because the radiosonde data are more accurate than data from the GPT+Bevis at sea. The RMS has the same varying trend as MAE, i.e. where the MAE is large, the RMS is also large. The RMS in oceanic areas is larger than that on land, and the RMS difference between land and sea is larger than the MAE difference. Results show that the modified GTm model can not only provide T_m in the global land areas with high accuracy, but also provide T_m in oceanic areas with a relatively high accuracy

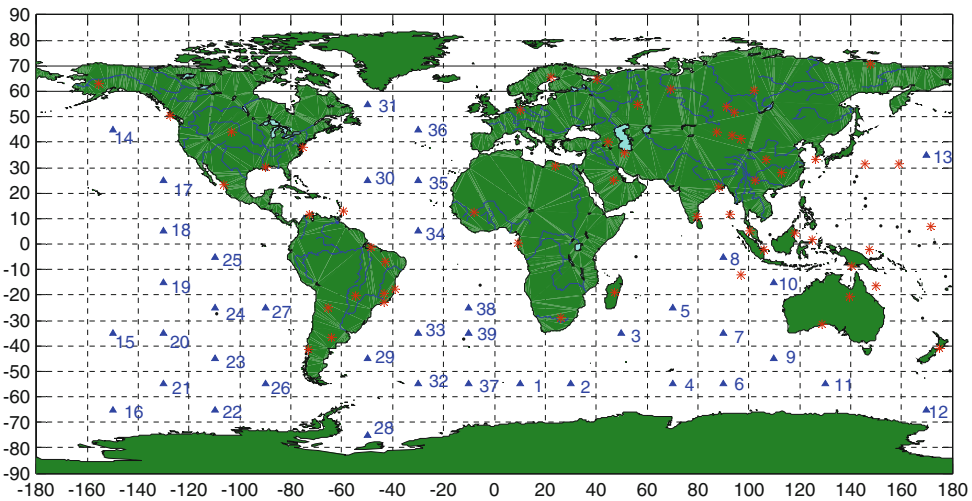

Fig. 6 The global distribution of 58 radiosonde stations and 39 ocean grids involved in external accuracy testing

Author's personal copy

and stability, indicating that the GTm-II model is globally applicable.

5.3 Comparison between GTm-I, GTm-II and Bevis T_m–T_s relationship

Internal and external accuracy tests described in Sect. 5.1 and Sect. 5.2 have preliminarily verified the accuracy and precision of the GTm-II model. To further test the advantages and disadvantages of the models and assess the accuracy of the GTm-II model comprehensively, GTm-I, GTm-II, and the Bevis T_m–T_s relationship were compared. The comparison was conducted as follows: T_ms from radiosonde data of 385 radiosonde stations or global COSMIC data in 2010 were considered as true values, and then MAE and RMS of the three models at each latitude were calculated. Results of comparison are shown in Fig. 8, and statistical results are shown in Table 1.

Figure 8a and b show that Bevis T_m–T_s relationship(T_s from GPT) has relatively large errors and appears to be unstable at mid and high latitudes of the northern hemisphere, but at low latitudes, it has smaller errors and appears to be stable. The GTm-I model turns out to be more stable in accuracy than the Bevis T_m–T_s relationship (T_s from GPT) and a little lower in accuracy than the GTm-II model and the Bevis T_m–T_s relationship (true T_s), despite a relatively poor accuracy at latitudes $N0°$ to $N20°$. South of 40° north latitude, the GTm-II model has a higher accuracy than the other three models, but appears to be less accurate than the Bevis T_m–T_s relationship(true T_s) north of N40°.

Figure 8c and d show that the accuracy of the GTm-I model is low, even abnormal south of N20°, which is just because less data in these areas were involved in the GTm-I modeling. However, the other models show a similar accuracy that is good and stable globally. This proves again that introducing T_m from GPT+Bevis to the GTm model could effectively improve the accuracy of the GTm model. We can also see that, north of N-60°, the GTm-II model shows a similar accuracy as the Bevis T_m–T_s relationship($_s$ from GPT),and the Bevis T_m–T_s relationship(true T_s) has a higher accuracy than the other three models. However, south of N-60°, the GTm-II model seems to be more stable and accurate than the other models. Detailed statistical data of the different models are shown in Table 1.

Table 1 shows that compared with radiosonde data, the GTm-II model is nearly as good as the Bevis T_m–T_s relationship (true T_s), and superior to the GTm-I model and Bevis T_m–T_s relationship (T_s from GPT). The GTm-I model is slightly more accurate than Bevis T_m–T_s relationship(T_s from GPT). When compared with the COSMIC data, the Bevis T_m–T_s relationship (true T_s) shows the highest accuracy of the four models, the GTm-II model shows a slightly higher accuracy than the Bevis T_m–T_s relationship (T_s from GPT). However, the accuracy of the GTm-I model is obviously low, just because a large part of the COSMIC occultations happened over the ocean, and it was not well constrained by the observations used to determine the coefficients of GTm-I at sea areas.

6 Comparison between GTm models and "GGOS Atmosphere" data

"GGOS Atmosphere" is a project aiming at establishing models of the atmosphere and its website provides T_m globally on $2° \times 2.5°$ grids every 6 h (http://ggosatm.hg.tuwien.ac.at/). The T_m is derived from data provided by European Centre for Medium-Range Weather Forecasts (ECMWF). To have a good understanding of the accuracy of the ECMWF T_m data, we checked them with radiosonde data in 2007 and COSMIC data in 2010 respectively. The results show that the "GGOS Atmosphere" Tm has a bias of 0.16 K and a RMS of 2.2 K compared with radiosonde data, and a bias of −0.06 K and a RMS of 1.94 K compared with COSMIC data, indicating that the ECMWF data have a high accuracy.

To further test the accuracy of the GTm-II model on a global scale, the "GGOS Atmosphere" data and the GTm-II model were compared. The sequential differences between the "GGOS Atmosphere" data and T_ms from GTm-II at 0:00, 6:00, 12:00 and 18:00UTC daily in 2010 was calculated, and then bias and MAE of the GTm-II model at each point of the grids were calculated. The global distribution of bias and MAE is shown in Fig. 9. Detailed statistical data of GTm-II are shown in Table 2.

Figure 9a shows that the GTm-II model is in good agreement with the "GGOS Atmosphere" data on a global scale. Except for small parts of the Antarctic region, Himalayas and Andes, the bias is no more than 6 K. Figure 9b shows that the bias near the polar regions is positive, but it becomes negative at sea areas near the equator and at some high altitudes (except the South Pole), especially in the Himalayan and Andes regions. Even so, the maximum bias is still less than 10.2 K.

Statistical results in Table 2 show that the global average bias of the GTm-II model is only −0.1 Kand the global MAE is only 3.6 K compared with the "GGOS Atmosphere" data, indicating that the GTm-II model agrees well with the "GGOS Atmosphere" data. So if the "GGOS Atmosphere" data have a high accuracy, so will the GTm-II model. By Comparing the GTm-I model and the GTm-II model, we can see the GTm-II model obviously improves the degree to which the GTm-I model conforms to the "GGOS Atmosphere" data.

The comparison of the GTm-II model and the "GGOS Atmosphere" data of high spatiotemporal resolution further reveals that the GTm-II model exhibits high accuracy and stability on a global scale.

Author's personal copy

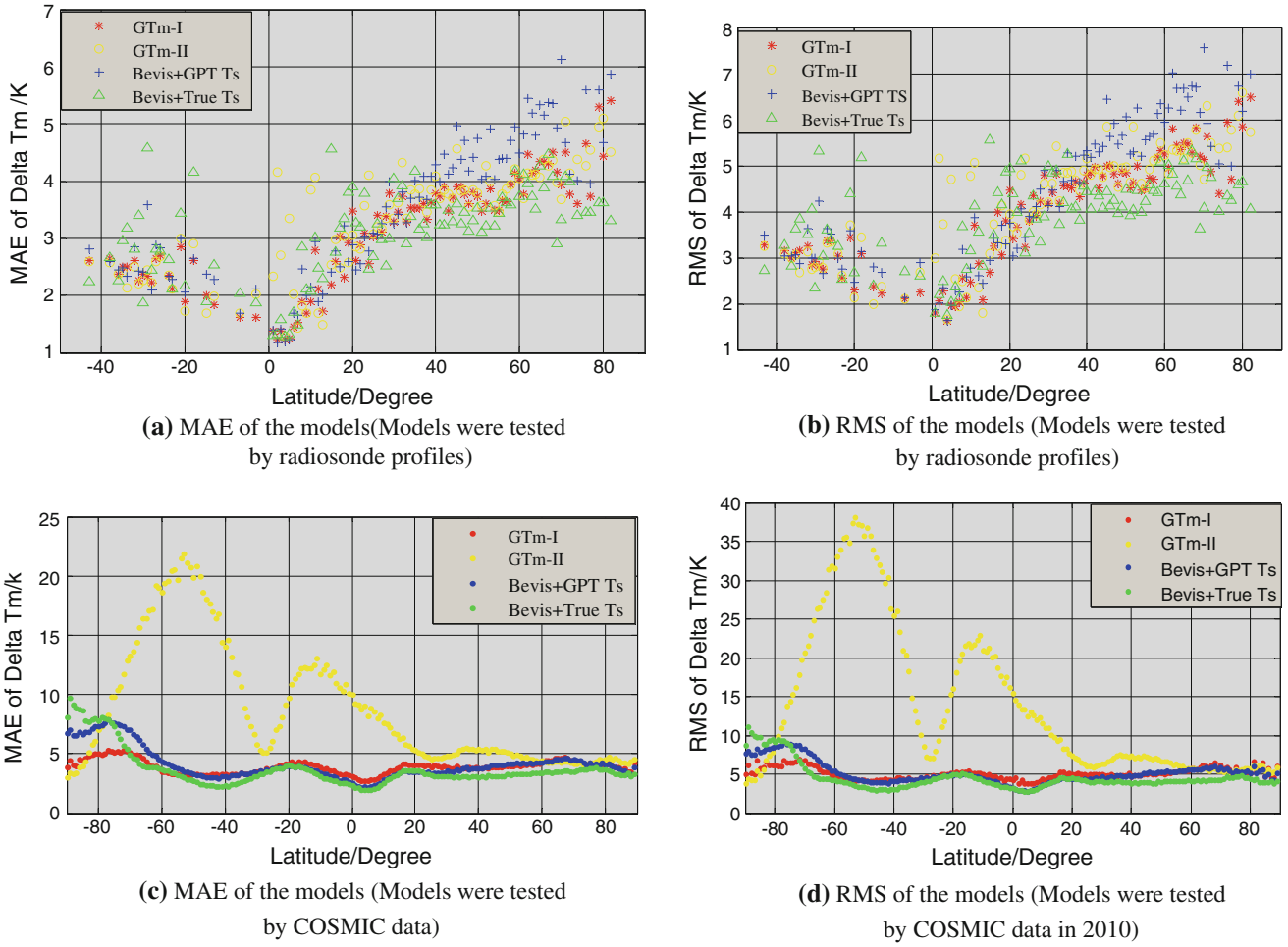

(a) MAE of the models(Models were tested by radiosonde profiles)

(b) RMS of the models (Models were tested by radiosonde profiles)

(c) MAE of the models (Models were tested by COSMIC data)

(d) RMS of the models (Models were tested by COSMIC data in 2010)

Fig. 8 Results of GTm-I, GTm-II, and the Bevis T_m–T_s relationship tested by radiosonde and COSMIC data in 2010

Table 1 Statistical results of different models tested by radiosonde and COSMIC data in 2010

	MAE (in Kelvin)			RMS (in Kelvin)		
	Mean	Max	Min	Mean	Max	Min
Compared with radiosonde data						
Bevis(True T_s)	3.1	4.6	1.3	3.9	5.6	1.8
Bevis(GPT)	3.5	6.1	1.2	4.4	7.6	1.6
GTm-I	3.3	5.1	1.3	4.2	6.6	1.7
GTm-II	3.1	5.4	1.2	4.0	6.5	1.6
Compared with COSMIC data						
Bevis(True T_s)	3.7	9.8	2.0	4.6	11.1	2.8
Bevis(GPT)	4.1	7.9	2.2	5.2	9.2	2.8
GTm-I	8.7	21.9	3.0	13.8	38.1	3.9
GTm-II	3.9	5.3	2.7	5.1	7.0	3.8

7 Conclusions

From the in-depth study of the GTm-I model, we found that the accuracy of the GTm-I model at sea cannot be ensured by employing spherical harmonics to determine the model coefficients in the absence of measured data in oceanic areas, and the bad structure of the equation during the modeling also affects the accuracy on land. In this paper, we have

Author's personal copy

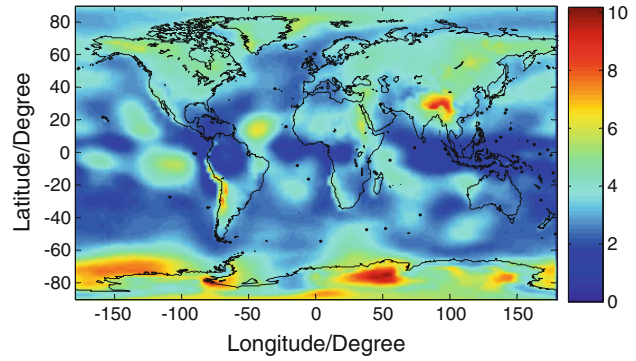

(a) Global MAE of GTm-II tested by "GGOS Atmosphere" data

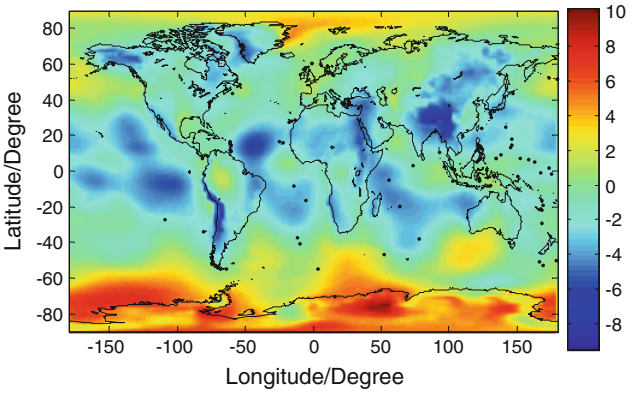

(b) Global bias of GTm-II tested by "GGOS Atmosphere" data

Fig. 9 Global error distribution of the GTm-II model compared with the "GGOS Atmosphere" data

Table 2 Bias and MAE of the GTm models compared with "GGOS Atmosphere" data

	Bias (in Kelvin)			MAE (in Kelvin)		
	Mean	Min	Max	Mean	Min	Max
GTm-I	2.0	−68.6	99.9	8.3	0	99.9
GTm-II	−0.1	−9.5	10.2	3.6	0.8	10.2

introduced virtual T_ms(T_ms from GPT+Bevis) to oceanic areas to solve the problem of data unavailability, and then recalculated the model coefficients by combining the radiosonde and virtual data. With this method, we have established the GTm-II model. Based on internal and external accuracy tests, we compared the GTm-II model and the "GGOS Atmosphere" data. The results indicate that the method of introducing virtual T_m to the GTm-II modeling not only solved the problem of low accuracy at sea but also improved the accuracy on land, making the GTm-II model more stable and a truly globally applicable model for estimating T_m.

Acknowledgments The authors would like to thank IGRA for providing access to the web-based IGRA data and "GGOS Atmosphere" for providing grids of T_m and COSMIC for the occultation data. This research was supported by the National Natural Science Foundation of China (41021061; 41174012;41274022).

References

Bevis M, Businger S, Chiswell S et al (1994) GPS meteorology: mapping zenith wet delays onto precipitable water. J Appl Meteorol 33:379–386

Bevis M, Businger S, Herring AT, et al. (1992) GPS meteorology: remote sensing of atmospheric water vapor using the global positioning system. J Geophys Res 97(D14):15787–15801

Boehm J, Heinkelmann R, Schuh H (2007) Short Note: a global model of pressure and temperature for geodetic applications. J Geod 81(10):679–683

Davis JL, Herring TA, Shapiro II, Rogers AEE, Elgered G (1985) Geodesy by radio interferometry: effects of atmospheric modeling errors on estimates of baseline length. Radio Sci 20:1593–1607

Ding JC (2009) GPS meteorology and its applications. China Meteorological Press, Beijing, pp 1–10

Gu XP (2004) Research on retrieval of GPS water vapor and method of rainfall forecast. Doctorial dissertation, China Agricultural University pp 1–15

Gu XP, Wang CY, Wu DX (2005) Research on the local algorithm for weighted atmospheric temperature used in GPS remote sensing water vapor. Sci Metero Sin 25(1):79–83

Kursinski ER, Syndergaard S, Flittner D et al (2002) A microwave occultation observing system optimized to characterize atmospheric water, temperature, and geopotential via absorption. J Atmos Oceanic Technol 19:1897–1914

Li JG, Mao JT, Li CC (1999) The approach to remote sensing of water vapor based on GPS and linear regression T_m in eastern region of China. Acta Meteor Sin 57(3):283–292

Li GP, Huang GF, Liu BQ (2006) Experiment on driving precipitable water vapor form ground-based GPS network in Chengdu Plain. Geomat Inf Sci 31(12):1086–1089

Lv YP, Yin HT, Huang DF (2008) Modeling of weighted mean atmospheric temperature and application in GPS/PWV of Chengdu region. Sci Survey Mapp 33(4):103–105

Liu YX, Chen YQ, Liu JN (2000) Determination of weighted mean tropospheric temperature using ground meteorological measurement. J Wuhan Techn Univ Survey Mapp 25(5):400–403

Mao JT (2006) Research of remote sensing of atmospheric water vapor using Global Positioning System (GPS). Doctorial dissertation, Beijing University pp 1–5

Rocken C, Ware R, Van Hove T, Solheim F, Alber C, Johnson J, Bevis M, Businger S (1993) Sensing atmospheric water vapor with the global positioning system. Geophys Res Lett 20(23):2631–2634. doi:10.1029/93GL02935

Ross RJ, Rosenfeld S (1997) Estimating mean weighted temperature of the atmosphere for Global Positioning System. J Geophys Res 102(18):21719–21730

Wang Y, Liu LT, Hao XG et al (2007) The application study of the GPS meteorology network in wuhan region. Acta Geodaet Cartogr Sinica 36(2):141–145

Yao YB, Zhu S, Yue SQ (2012) A globally applicable, season-specific model for estimating the weighted mean temperature of the atmosphere. J Geod 86:1125–1135. doi:10.1007/s00190-012-0568-1

Yu SJ (2011) Remote sensing of water vapor based on Ground GPS observations. Doctor thesis, Institute of Geodesy and Geophysics, Chinese Academy of Sciences, Wuhan, pp 37–50